Parameter study on factors influencing wave-induced liquefaction

H. Keese
Geotechnical Institute, TU Bergakademie Freiberg, Freiberg, Germany, hannah.keese@ifgt.tu-freiberg.de

J. Rothschink, O. Stelzer
Federal Waterways Engineering and Research Institute, Karlsruhe, Germany

T. Nagel
Geotechnical Institute, TU Bergakademie Freiberg, Freiberg, Germany, thomas.nagel@ifgt.tu-freiberg.de
Freiberg Center for Water Research (ZeWaF), TU Bergakademie Freiberg, Freiberg, Germany

ABSTRACT: Wave-induced liquefaction, whereby the behaviour of soil changes from solid-like to fluid-like, can lead to sediment movement, destabilisation of bank protection measures or washout of submarine pipelines, due to the loss of soil's load-bearing capacity. This process is influenced by various parameters, such as the permeability of the soil and the degree of saturation. Before conducting a numerical simulation, the different input parameters must be determined. It is good practice to investigate how much the uncertainty of these input parameters influences the results of the numerical simulation. This paper presents a parameter study analysing the extent of the dependency between the uncertainty of the input parameters and the numerical result. Hydraulic conductivity, stiffness, degree of saturation and porosity were chosen as the parameters to be analysed, and the results were compared in terms of liquefaction depth.

The setup is based on a soil column experiment in combination with an alternating flow apparatus that replicated a liquefaction event caused by a linear pressure drawdown. Prior to the parameter study, good agreement is demonstrated between the numerical simulation and the experimental analysis. Simulations are based on a total Lagrangian formulation.

1 INTRODUTION – WAVE-INDUCED LIQUEFACTION

Liquefaction is a process that has attracted the interest of many researchers worldwide due to its potential consequences, such as sediment movement, destabilization of bank protection measures or washout of submarine pipelines to name just the ones of interest in the area of wave-induced liquefaction. This process where the soil turns from solid-like behaviour to fluid-like behaviour is influenced by several parameters. Huang et al. (2015) distinguishes influencing factors between wave characteristics like water depth or wave height and soil characteristics like permeability or degree of saturation. As part of their research many researchers conduct a parametric analysis after their numerical simulations or their experimental analyses. Based on this, they conclude that there are specific limit values, such as a hydraulic conductivity above which no liquefaction occurs (Liu et al. 2009). However, dependencies found based on simulations or experiments often contradict each other. One parameter that often led to different results is the degree of saturation: Huang et al. (2015) for example states that soil with a higher degree of saturation (lower gas) is more likely to liquefy because of the absence of compressible gas. In contrast to that Ye et al. (2015) analysed a lower liquefaction potential with a higher degree of saturation.

This publication first compares experimental findings based on a linearized drawdown test conducted in a soil column – which are analysed in detail by Rothschink et al. (2026) – with a numerical simulation. A parametric study based on numerical simulations follows, along with an analysis of the boundary conditions that led to the specific correlations and the factors that restrict the generalisation of the results. The focus is on hydraulic conductivity, stiffness, degree of saturation, and porosity. Due to the boundary conditions of the experimental dataset, this publication addresses momentary liquefaction, which occurs when the soil is temporarily liquefied during the wave trough phase due to a delayed response in pore water pressure (Sakai et al. 1992). The wave trough phase corresponds to the period during and after the drawdown in the experiment, when the pore water pressure in the soil does not decrease as quickly as the boundary conditions at the soil surface.

2 DATA BASE AND METHODS

2.1 Hydro-mechanical model

Wave-induced liquefaction simulation needs a strong hydro-mechanical coupling, a variable permeability and the possibility for finite deformation. A process model with the necessary kinematic description and process coupling but simple constitutive approaches was set up within the FEniCS framework (Alnaes et al. 2015, Logg et al. 2012). For detailed information on the model see Keese et al. (2025); its most important aspects will be replicated here to provide a context for the reader.

The first weak formulation governs the mechanical response of the body due to body forces and surface traction

$$\int_{\Omega_0} \boldsymbol{S}_{\mathrm{s}}^{\mathrm{E}} : \delta \boldsymbol{E}_{\mathrm{s}} \mathrm{d}\Omega_0 - \int_{\Omega_0} p J_{\mathrm{s}} \boldsymbol{C}_{\mathrm{s}}^{-1} : \delta \boldsymbol{E}_{\mathrm{s}} \mathrm{d}\Omega_0 - \int_{\Omega_0} \rho_0 \boldsymbol{g} \cdot \boldsymbol{v}_u \mathrm{d}\Omega_0 - \int_{\partial\Omega_{0\bar{t}}} \bar{\boldsymbol{t}} \cdot \boldsymbol{v}_u \mathrm{d}\Gamma_0 = 0 \quad \forall \boldsymbol{v}_u \in \boldsymbol{V}_u, \tag{1}$$

where $\boldsymbol{S}_{\mathrm{s}}^{\mathrm{E}}$ is the effective Second Piola Kirchhoff stress (Pa) , $\delta \boldsymbol{E}_{\mathrm{s}}$ is the linearization of the Green-Lagrange strain tensor in the direction of the test function $\boldsymbol{v}_u$, J_{s} is the determinant of the deformation gradient, $\boldsymbol{C}_{\mathrm{s}}^{-1}$ is the inverse of the Right Cauchy Green tensor, ρ_0 is the reference bulk mass density (kg/m³), $\boldsymbol{g}$ the gravitational acceleration (m/s²) and $\bar{\boldsymbol{t}}$ the surface traction (Pa) specified on the Neumann boundary.

The second weak formulation governs the hydraulical part of the model

$$\int_{\Omega_0} \rho^{\mathrm{fR}} J_{\mathrm{s}} \boldsymbol{C}_{\mathrm{s}}^{-1} : \dot{\boldsymbol{E}}_{\mathrm{s}} v_p \mathrm{d}\Omega_0 + \int_{\Omega_0} \rho^{\mathrm{fR}} \mathrm{Grad}\, v_p \cdot \boldsymbol{K} \mathrm{Grad}\, p \, \mathrm{d}\Omega_0 - \int_{\Omega_0} (\rho^{\mathrm{fR}})^2 \mathrm{Grad}\, v_p \cdot \boldsymbol{K} \boldsymbol{g} \boldsymbol{F}_{\mathrm{s}} \mathrm{d}\Omega_0 + \int_{\Omega_0} J_{\mathrm{s}} \rho^{\mathrm{fR}} n^{\mathrm{f}} \beta_p \dot{p} v_p \mathrm{d}\Omega_0 - \int_{\partial\Omega_{0Q}} \rho^{\mathrm{fR}} Q v_p \mathrm{d}\Gamma_0 = 0 \; \forall v_p \in V_p, \tag{2}$$

where ρ^{fR} is the material density of the fluid (kg/m³), $\dot{\boldsymbol{E}}_{\mathrm{s}}$ the material time derivative of the Green-Lagrange strain tensor (1/s), v_p the test function, $\boldsymbol{K}$ the specific permeability (m²/(Pa s)), $\boldsymbol{F}_{\mathrm{s}}$ the deformation gradient, n^{f} the porosity, β_p the pore fluid compressibility (1/Pa), $\dot{p}$ the time derivative of the pore water pressure (Pa/s) and Q the fluid flux across the boundary (m³/m²s).

These two weak formulations, set up in a Total Lagrangian framework, allow the two unknowns $\boldsymbol{u}$ – the displacement vector – and p – the pore water pressure – to be determined. However, constitutive equations are required to describe the stress-strain relation, the permeability and the density evolution. For the first one – the stress strain relation – a simple hyper-elastic compressible Neo-Hookean approach is combined with a tension cut-off.

The permeability model incorporates the assumption of a monodisperse particle structure

$$\boldsymbol{k} = \frac{d^2}{18 n^{\mathrm{s}} (1 - n^{\mathrm{s}}) \mu_{\mathrm{fR}} \hat{F}(n^{\mathrm{s}}, \mathrm{Re} \to 0)} \boldsymbol{I}, \tag{3}$$

Where $\boldsymbol{k}$ is the specific permeability in the current configuration (m²/(Pa s)), d is the particle diameter (m), n^{s} the solid phase volume fraction, μ_{fR} the fluid viscosity (Pa s) and $\hat{F}(n^{\mathrm{s}}, \mathrm{Re} \to 0)$ the normalized drag force function for negligible Reynolds numbers. For the normalized drag force function $\hat{F}(n^{\mathrm{s}}, \mathrm{Re} \to 0)$, an expression developed by Van der Hoef et al. (2005) is included:

$$\hat{F}(n^{\mathrm{s}}, \mathrm{Re} \to 0) = \frac{10 n^{\mathrm{s}}}{(1 - n^{\mathrm{s}})^2} + (1 - n^{\mathrm{s}})^2 (1 + 1.5\sqrt{n^{\mathrm{s}}}). \tag{4}$$

The effective momentum production term derived by Baumgarten and Kamrin (2019) equipped by Eq. (4) was used to derive Eq. (3) in Keese et al. (2025). After a pull-back of Eq. (3) it can be used as the non-constant permeability $\boldsymbol{K}$ in the second weak formulation.

To account for compressibility of the pore fluid, a pressure-dependent density model was applied:

$$\rho^{\mathrm{fR}} = \rho_{\mathrm{ref}}^{\mathrm{fR}} \exp\left[\beta_p (p - p_{\mathrm{ref}})\right], \tag{5}$$

including a reference density $\rho_{\mathrm{ref}}^{\mathrm{fR}}$ (kg/m³) at reference pressure p_{ref} (Pa) and the compressibility β_p (1/Pa) itself. The compressibility has to be taken into account because of the quasi-saturated conditions apparent in riverbeds.

2.2 Experimental setting

The Federal Waterways Engineering and Research Institute in Germany developed a test apparatus for alternating flow in combination with a soil column which can be filled with different soil types (Kayser et al. 2016). The cell itself is 0.328 m in diameter and was filled to a height of 0.855 m in the test case analysed below. The test apparatus for alternating flow is a pneumatic-hydraulic system. Within the system in two pressure tanks a membrane separates water and air, enabling pressure to be applied to the water phase. This specific pressure represents a particular water column above the soil surface which then can be reduced computer-controlled at a specific rate to imitate a change in water level. With this set-up drawdown-induced liquefaction can be investigated in a controllable setting. If realistic water bed conditions are to be reproduced, quasi-saturated conditions are created by the sample manufacturing technique of water pluviation with subsequent compaction using a hammer, then draining the water and afterwards resaturating the sample. The column itself is equipped with nine piezo-resistive pressure sensors evenly distributed along the column height. Due to this spacing a statement regarding the pore water pressure evolution with depth is possible. For a detailed explanation of the test apparatus see Kayser et al. (2016), for sample preparation see Rothschink and Stelzer (2022) and for data evaluation of liquefaction experiments see Rothschink et al. (2026).

Table 1 shows the input parameters of the process model and the included constitutive approaches. The effective particle diameter related to the monodisperse assumption is no parameter taken from a grain size distribution but a secondary parameter calculated by means of Eq. (3) as:

$$d = \sqrt{k_\mathrm{s} \cdot 18 \cdot n^\mathrm{s} \cdot (1 - n^\mathrm{s}) \cdot \hat{F}(n^\mathrm{s}, \mathrm{Re} \to 0)}, \tag{6}$$

including the intrinsic permeability k_s (m²). The solid phase volume fraction that is needed for Eq. (6) can be calculated using the saturation condition ($n^\mathrm{s} + n^\mathrm{f} = 1$) and the equation for the porosity evolution (Görke et al. 2009)

$$n^\mathrm{f} = 1 - \frac{1-n^{\mathrm{f}0}}{J_\mathrm{s}}, \tag{7}$$

where $n^{\mathrm{f}0}$ is the initial porosity which can be derived from the installed mass as well as the height and diameter of the sand column. Eq. (7) is also used within the simulation to update the porosity while the particle diameter is set constant throughout one complete simulation. The intrinsic permeability k_s (m²) in Eq. (6) is derived from experimentally obtained hydraulic conductivity values accounting for a temperature correlation via:

$$k_\mathrm{s} = \frac{k_\mathrm{f}(T) \cdot \mu_\mathrm{fR}(T)}{\rho_\mathrm{fR}(T) \cdot g}, \tag{8}$$

and (DIN-Normenausschuss Bauwesen 2021):

$$k_\mathrm{f}(T) = \frac{\mu_\mathrm{fR}\left(T_{k_\mathrm{f}-\mathrm{test}}\right)}{\mu_\mathrm{fR}(T)} \cdot k_\mathrm{f}(T_{k_\mathrm{f}-\mathrm{test}}). \tag{9}$$

The fluid viscosity in Eq. (8) and (9), which is also temperature dependent, can be calculated using the following equation (DIN-Normenausschuss Bauwesen 2021):

$$\mu_\mathrm{fR}(T) = 0.02414 \cdot 10^{\left[\frac{247.8}{T/^\circ C + 133}\right]} \cdot 10^{-3} \quad \mathrm{Pa\ s}. \tag{10}$$

Additional to the parameters explained above, the compressibility is needed which can be calculated under partially saturated conditions as (Fredlund 1976):

$$\beta_p = S_\mathrm{r}\beta_\mathrm{w} + \frac{1-S_\mathrm{r}}{p} + \frac{S_\mathrm{r} h}{p}, \tag{11}$$

with degree of saturation $S_\mathrm{r} = 0.927$, pure water compressibility $\beta_\mathrm{w} = 4.81 \cdot 10^{-7}$ m²/kN (inverse of the bulk modulus of pure water $K_\mathrm{w} = 2.08 \cdot 10^{9}$ Pa) (Ewers and Karl 2017), mean pressure $p = 1.4968 \cdot 10^{5}$ Pa and Henry constant $h = 0.02$.

Table 1: Input parameters of the process model and the included constitutive approaches.

Parameter	Symbol / Unit	Value V33
Density of the soil particles	ρ^{sR}/ kg m^{-3}	2650
Young's modulus	E / Pa	$2.26 \cdot 10^{7}$
Poisson's ratio	ν	0.3
Particle diameter	d / m	0.000036
Initial porosity	$n^{\mathrm{f}0}$	0.4472
Hydraulic conductivity during k_f-test	$k_\mathrm{f}(T_{k_\mathrm{f}\text{-test}})$ / ms^{-1}	$1.182 \cdot 10^{-4}$
Temperature during k_f-test	$T_{k_\mathrm{f}\text{-test}}$ / °C	26.86
Temperature	T / °C	27.99
Fluid density at reference pressure	$\rho^{\mathrm{fR}}_{\mathrm{ref}}$ / kg m^{-3}	996.2
Reference pressure	p_ref / Pa	101,325
Fluid compressibility	β_p / Pa^{-1}	$6.12 \cdot 10^{-7}$
Degree of saturation	S_r	0.927

Next to the parameter symbols and their units, Table 1 also shows the specific values of one drawdown experiment. Dataset V33 represents the soil reaction to a linearized ship-induced drawdown of 0.12 ms^{-1} in 10 s. The initial and final pressure values are 155.28 kPa and 143.35 kPa, respectively. The following Figure 1 shows the excess pore water pressure with depth calculated from the measured values as dots. Additionally, the numerical results are shown as solid lines. It becomes apparent that the numerical results honour the theoretical limit shown by the dashed curve $\gamma' z$ and reproduce the experimental results. The point in space where the numerical result departs from the theoretical maximum given by suspension weight can be seen as the liquefaction front or the liquefaction depth z_{l}. This point is marked as a cross in Figure 1. At the end of the drawdown $(t_0 + 10\,\mathrm{s})$ the maximum excess pore water pressure is reached corresponding to the maximal liquefaction depth of 0.506 m.

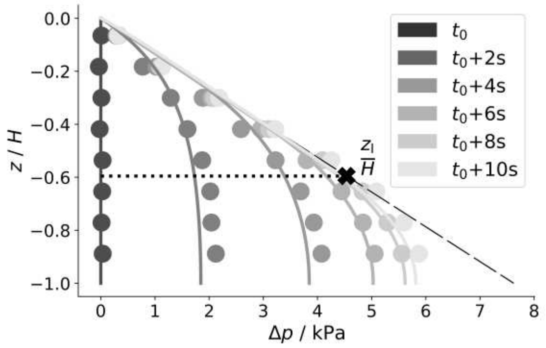

Figure 1: Excess pore water pressure development throughout the experiment (dots) and the simulation (solid line) for a column of height H = 0.855 m.

2.3 Parametric study

Seabed liquefaction is influenced by several parameters which are pointed out in the introduction. The literature review also shows that researchers do not always agree on the effect of a specific parameter.

This parametric study should therefore comprise several parts. In the first part the stiffness, porosity, degree of saturation and hydraulic conductivity are varied systematically to obtain a data pool. Table 2 shows the mean values which are kept while other parameters are varied and the min/max of each parameter under consideration. Every correlation is based on conditions and assumptions. The following first simulations are bounded by the drawdown rate given by V33 and the column height of 0.85 m. In a second step the height of the column is expanded to analyse the influence of the column height on the correlations obtained. In a third step the shown correlations should be made more general and put into the context of Terzaghi's analytical consolidation theory.

Table 2. Parameters used for the parametric study. As underlaying distribution, a normal distribution was chosen for every parameter except the hydraulic conductivity where a log-normal distribution was chosen for derivation of the mean value.

Parameter	Symbol / Unit	Mean	Max	Min
Stiffness (1)	E / Pa	$2.04\cdot10^{7}$	$3.71\cdot10^{7}$	$0.37\cdot10^{7}$
Porosity (2)	n^{f0}	0.467	0.52	0.414
Degree of saturation (1)	S_{r}	0.9	0.95	0.85
Hydraulic conductivity (3)	k_{f} $(T_{k_{\mathrm{f}}\text{-test}})$/ ms^{-1}	$3.15\cdot10^{-5}$	$1\cdot10^{-3}$	$1\cdot10^{-6}$

(1) (Köhler 1997)
(2) Laboratory experiments
(3) (Boley et al. 2012)

3 RESULTS – PARAMETRIC STUDY

All correlations analysed hereafter are compared in terms of the liquefaction depth z_{l}. As illustrated in Figure 1, the liquefaction depth is the point at which the solution deviates from the theoretical limit. The simulation results adhere to the theoretical limit due to the tension cut-off. The transition point at which the Cauchy stress becomes non-zero is therefore set as the liquefaction depth in post-processing.

3.1 Boundary conditions of V33

The following three figures (Figure 2-Figure 4) show contour plots of the cross correlations $k_{\mathrm{f}} - E$, $k_{\mathrm{f}} - S_{\mathrm{r}}$, and $k_{\mathrm{f}} - n$. They are created based on an interpolation of the single data points shown as crosses. The colours are indicating the resulting liquefaction depth.

Figure 2 shows nearly vertical lines that illustrate the stronger influence of the hydraulic conductivity than the Young's modulus. By contrast, Figure 3 depicts a shift whereby higher saturation values demonstrate lower liquefaction depths than lower saturation values at the same hydraulic conductivity. This difference increases with increasing hydraulic conductivity until it evens out in the absence of liquefaction. Figure 4 can be considered to lie between Figure 2 and Figure 3. The lines indicate a slight tendency for higher porosities to exhibit a slower decrease in liquefaction depth with increasing hydraulic conductivity than lower porosities.

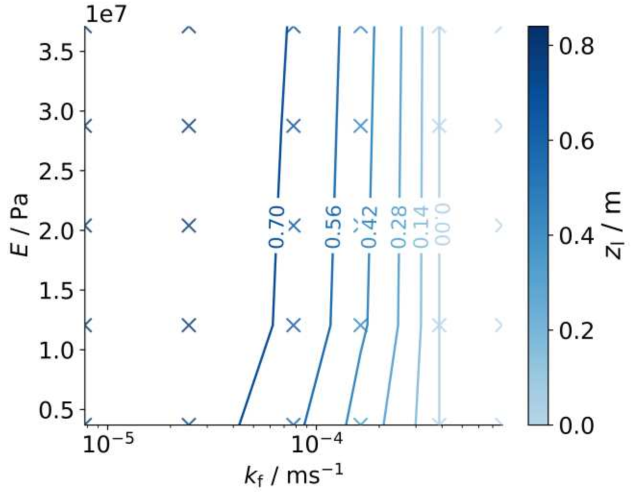

Figure 2: Contour plot of the cross correlation between hydraulic conductivity and Young's modulus.

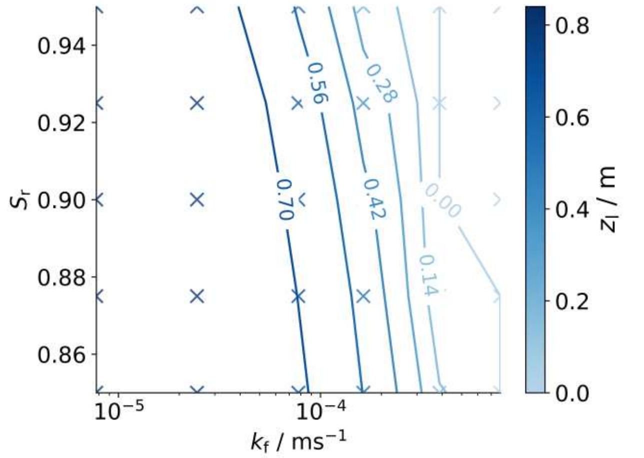

Figure 3: Contour plot of the cross correlation between hydraulic conductivity and degree of saturation.

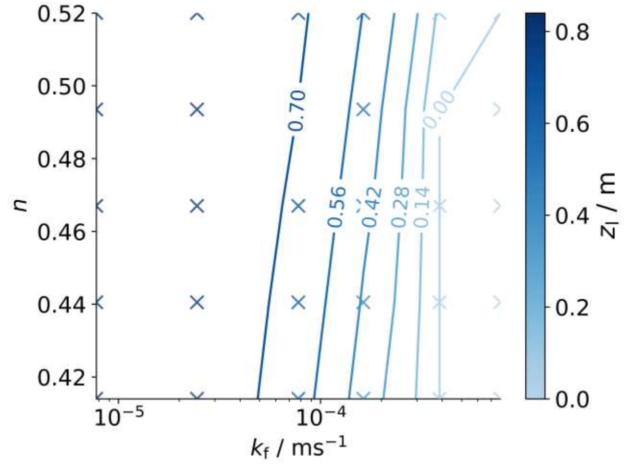

Figure 4: Contour plot of the cross correlation between hydraulic conductivity and porosity.

3.2 Influence of the column height

In a second step the column height was expanded to analyse its effect on the numerical simulation. All the simulations shown in Section 3.1 were conducted with a column length of 0.85 m, as this was the height of the soil column in the experiment. Figure 5 shows on the one hand the pore water pressure at the end of the drawdown in a 0.85 m soil column, as indicated by the lighter grey dotted line. In comparison to Figure 1 the x-axis is now also normalized – Section 2.2 provides the overall magnitude of the pressure drawdown as 11.9 kPa. This value will be named p_{DD} hereafter with the index DD for drawdown. In addition to the result of a column height of 0.85 m, Figure 5 shows the result of a column height of 2.5 m as darker grey dotted line. It becomes apparent, that a higher excess pore water pressure is reached than in the lower column.

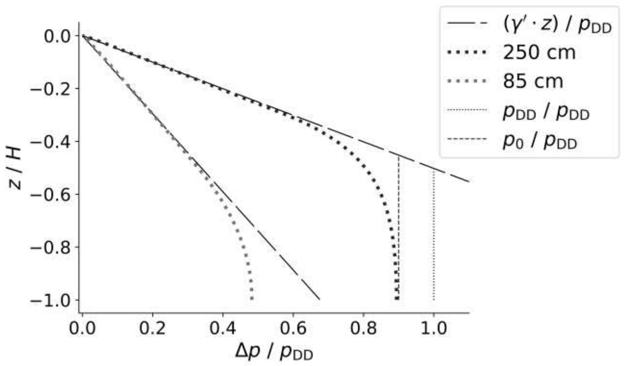

Figure 5: A comparison of the development of excess pore water pressure in relation to the column length.

The differences in the results can be attributed to boundary effects that limit the liquefaction depth and prevent it from spreading to the physically possible liquefaction depth at the given drawdown p_{DD}. Nevertheless, the curve of the 2.5 m column still does not reach $p_{\mathrm{DD}}/p_{\mathrm{DD}}$. The reason for this observation is an instantaneous pore water pressure relaxation associated with expansion of the compressible fluid during unloading of the soil column. To illustrate this, a p_0/p_{DD} curve was added to Figure 5, calculated from consolidation theory as

$$p_0 = p_{\mathrm{DD}} - \frac{p_{\mathrm{DD}}}{1+E_s \beta n}, \qquad (12)$$

considering the maximum pressure difference of the external load (Pa), the stiffness modulus (Pa), the porosity as well as the fluid compressibility (1/Pa). Figure 5 shows that the excess pore water pressure of the soil column of 2.5 m reaches the p_0/p_{DD} curve. Additional simulations showed that a further increase in soil column height does not change the maximum excess pore water result any more.

This result shows that the column height influences the numerical result as long as boundary effects influence the resulting pressure profiles. Because consolidation theory provides a good basis for interpreting the results of the excess pore water pressure, in the next section, it should be used in order to discuss general and straight-forward estimates of the liquefaction depth.

3.3 Interpretation based on consolidation theory

The one-dimensional consolidation equation of a Terzaghi model can be solved analytically for a linear-ramp-and-hold type loading, matching the conditions of the present study. In Section 2.2 the overall change of the water load is given by 11.9 kPa between the initial pressure and the pressure after the linearized drawdown. This load is applied within 10 s due to the inclination of the load change in the experiment. The following figures always show the end of this linear pressure ramp for different parameter combinations. Each figure shows the depth normalized by the column height over the excess pore water pressure normalized by the magnitude of the drawdown pressure. Figure 6 shows results depending on the compressibility. During the calculation each parameter stays the same except the compressibility of the pore fluid and the initial density. The colour of the consolidation line corresponds to the colour of the $(\gamma' z)/p_{\mathrm{DD}}$ curve. Between every pair the intersection point was calculated as well as marked in the plot indicating the maximal liquefaction depth for each parameter constellation. It becomes apparent that the liquefaction depth decreases with decreasing β. This means that liquefaction is reduced when saturation is higher. The left-most consolidation curve shows no excess pore water pressure. This curve corresponds to the compressibility of water-saturated soil. In Figure 6 there are also several vertical dashed lines corresponding to the theoretical initial overpressures calculated from Eq. (12) which is always inferior to $p_{\mathrm{DD}}/p_{\mathrm{DD}}$ for the chosen parameter sets.

Taking this procedure one can think of testing other parameter dependencies. Figure 7 shows the same procedure but for different hydraulic conductivities. The parameter set with the lowest hydraulic conductivity reaches the p_0/p_{DD} curve the closest and shows the maximum liquefaction depth in comparison with the other shown values. As the hydraulic conductivity increased, the liquefaction depth decreases until it becomes zero in the end and departing from the p_0/p_{DD} curve. A similar picture can be generated by varying the drawdown rate. In Figure 7 additionally the numerical results without tension cut-off are shown as dotted lines. It becomes apparent that the curves match quite well with the consolidation theory.

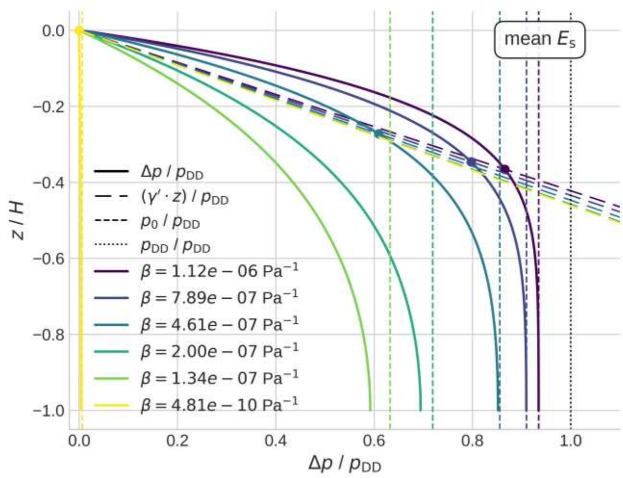

Figure 6: Excess pore water pressure with depth arising from consolidation theory depending on beta.

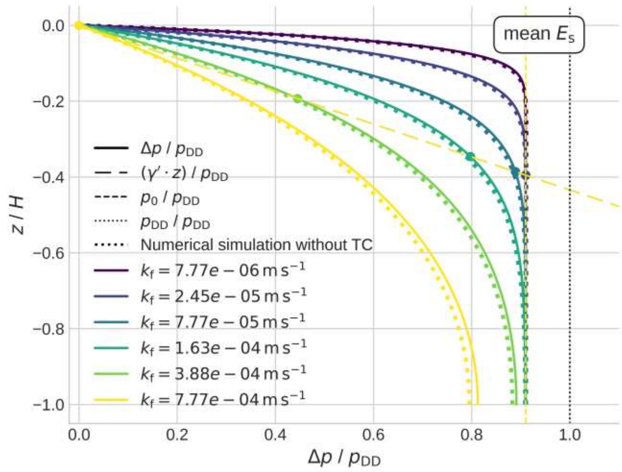

Figure 7: Excess pore water pressure with depth arising from consolidation theory (solid lines) depending on the hydraulic conductivity in comparison with numerical results without tension cut-off (dotted lines).

In the contour plots shown in Section 3.1, cross correlations can be observed. The next two figures (Figure 8 and Figure 9) are based on the same parameter constellations as Figure 7 with the difference that not the mean stiffness but instead the minimum stiffness (in Figure 8) and the maximum stiffness (in Figure 9) are used. It becomes apparent that not the tendency between the curves have changed, but the p_0/p_{DD} curve changes, leading to different liquefaction depths.

Additionally, in Figure 9 the numerical results are plotted but this time with an active tension cut-off. As in Figure 7 good agreement can be seen but some deviations get apparent in curve three and four from the left. The curves are not as steep as the consolidation theory leading to a lower liquefaction depth. This would mean that consolidation theory can be used to map the maximum liquefaction depth particularly under rapid drawdowns (or low permeabilities) while at slow drawdowns (or high permeabilities) forecast no liquefaction.

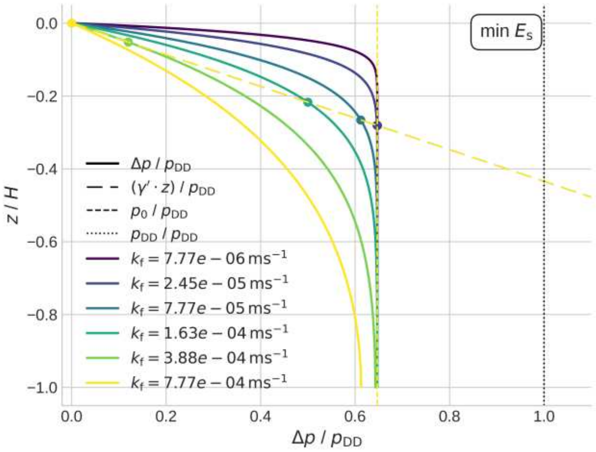

Figure 8: Excess pore water pressure with depth arising from consolidation theory depending on the hydraulic conductivity with minimum stiffness.

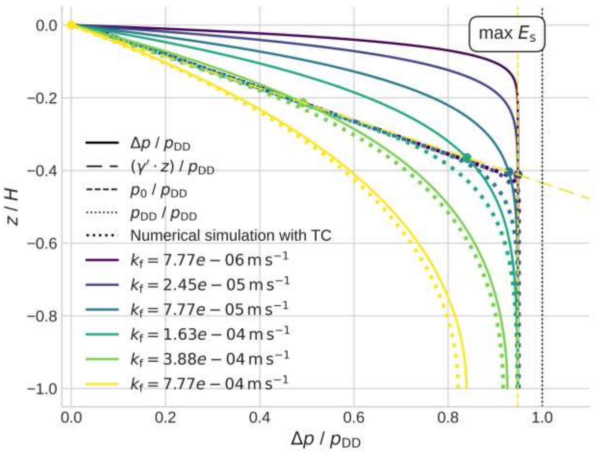

Figure 9: Excess pore water pressure with depth arising from consolidation theory (solid lines) depending on the hydraulic conductivity with maximum stiffness in comparison with numerical results with tension cut-off (dotted lines).

4 DISCUSSION

Although different limiting effects are analysed in this publication, the ranges of values chosen in Table 2 do not take into account that the behaviour of the soil changes due to liquefaction from solid-like to fluid-like and that the usual ranges of fine sand may be extended from the moment of liquefaction. This would have an effect on the interpretation if it is not only the maximum extent of liquefaction that is considered, but also how quickly resedimentation occurs. While the porosity and the permeability are intrinsically updated during the simulation due to the model components (see Eq. (3) and (7)), this is not the case for the stiffness and the degree of saturation. Since the degree of saturation already covers a large range, the authors consider stiffness to be the parameter that requires more detailed consideration in terms of the value range if the interpretation is to be extended to the post-liquefaction period.

The stiffness of the soil during liquefaction and in the resedimentation period is treated differently in literature. While some researchers set the stiffness in the liquefied area to zero, others distance themselves from this theory of disappearing stiffness and introduce, for example, a transition zone in which no effective stresses are yet present, but stiffness is taken into account (Miyamoto et al. 2004). Furthermore, it is discussed that the stiffness in the area of reconsolidation cannot be set as constant, as in Terzaghi‘s theory – For example, Adamidis and Madabhushi (2016) calculate the stiffness using different equations, each of which depends on the magnitude of the effective stress and the void ratio e.

The currently selected constitutive components of the model do not include a variable stiffness to the extent described.

5 CONCLUSIONS

This publication shows that the manner in which model parameters influence the liquefaction depth and excess pore water pressure profiles also depends on experimental or in-situ boundary conditions such as the column height. If the physical process cannot evolve freely but instead is influenced by boundary effects the results can be biased.

Consolidation theory was additionally used to test whether conclusions can be made regarding the liquefaction depth by calculating the intersection point between the analytically calculated excess pore water pressure and the limiting curve $\gamma' z$. The results show a quite good match with the numerical simulation for fast or slow drawdowns, while differences occur in an intermediate range in which the effective stress loss at liquefaction alters the excess pore water pressure curves. Nevertheless, the consolidation theory consistently shows a higher liquefaction depth reflecting a conservative result. Consolidation theory can therefore be used for a first estimation of the maximum liquefaction depth and the maximum excess pore water pressure possible. Besides that, it is possible to analyse correlations between different parameters via their contribution to the consolidation coefficient.

ACKNOWLEDGEMENTS

The first author acknowledges funding provided by the German Federal Waterways Engineering and Research Institute.

REFERENCES

Adamidis, O. and Madabhushi, G. S. (2016). Post-liquefaction reconsolidation of sand. *Proceedings of the Royal Society A: Mathematical, Physical and Engineering Sciences.* https://doi.org/10.1098/rspa.2015.0745

Alnaes, M. S., Blechta, J., Hake, J., Johansson, A., Kehlet, B., Logg, A., Richardson, C., Ring, J., Rognes, M., and Wells, G. (2015). The FEniCS project version 1.5. *Archive of Numerical Software 3*(100): 9–23. https://doi.org/10.11588/ans.2015.100.20553

Baumgarten, A. S. and Kamrin, K. (2019). A general fluid-sediment mixture model and constitutive theory validated in many flow regimes. *Journal of Fluid Mechanics*, 861: 721-764. https://doi.org/10.1017/jfm.2018.914

Boley, C., Adam, D., Bente, S., Börger, R., Dausch, G., Englert, K., Entenmann, W., Ferrari, H., Fuchs, B., Haack, A., Marte, R., Meier, C., Meyer, F., Morgen, K., Paulus-Grill, M., Scharinger, F., Schmitz, S., Schuppender, B., Stelzig, S., ... Zou, Y. (2012). Handbuch Geotechnik – Grundlagen – Anwendungen – Praxiserfahrungen. Geotechnical Engineering Handbook – Fundamentals – Applications – Practical Experience. *Springer*, (in [German]).

DIN-Normenausschuss Bauwesen (2021). DIN EN ISO 17892-11:2021-3, Geotechnische Erkundung und Untersuchung – Laborversuche an Bodenproben – Teil 11: Bestimmung der Wasserdurchlässigkeit (ISO 17892-11:2019); Deutsche Fassung EN ISO 17892-11:2019. Geotechnical investigation and testing – Laboratory testing of soil – Part 11: Permeability tests. www.beuth.de, (in [German]).

Ewers, J. and Karl, F. (2017). Determining fluid compressibility and soil permeability of quasi saturated sand with the alternating flow apparatus. *Springer Series in Geomechanics and Geoengineering*, 239-246. https://doi.org/10.1007/978-3-319-52773-4_27

Fredlund, D. G. (1976). Density and compressibility characteristics of air-water mixtures. *Canadian Geotechnical Journal*, 13: 386-396. www.nrcresearchpress.com

Görke, U.-J., Kaiser, S., Bucher, A. and Kreißig, R. (2009). Ein Beitrag zur gemischten Finite-Elemente-Formulierung der Theorie gesättigter poröser Medien bei großen Verzerrungen. A contribution to the mixed finite element formulation of the theory of saturated porous media under large deformation. http://www.tu-chemnitz.de/mathematik/csc/, (in [German]).

Huang, Y., Bao, Y., Zhang, M., Liu, C. and Lu, P. (2015). Analysis of the mechanism of seabed liquefaction induced by waves and related seabed protection. *Natural Hazards*, 79(2): 1399-1408. https://doi.org/10.1007/s11069-015-1897-1

Kayser, J., Karl, F., Schürenkamp, D., Schwab, N., Oumeraci, H. (2016). A test apparatus for alternating flow in geotechnical engineering. *Geotechnical Testing Journal* 39(5): 865-878. https://doi.org/10.1520/GTJ20150252

Keese, H., Rothschink, J., Stelzer, O. and Nagel, T. (2025). Transient hydro-mechanical analyses of column experiments on wave-induced soil liquefaction. *Computers and Geotechnics*, 185. https://doi.org/10.1016/j.compgeo.2025.107321

Köhler, H.-J. (1997). Boden und Wasser – Druck und Strömung. Soil and water – pressure and flow. *Mitteilungsblatt der Bundesanstalt für Wasserbau 76*, (in [German]).

Liu, Z., Jeng, D. S., Chan, A. H. C. and Luan, M. (2009). Wave-induced progressive liquefaction in a poro-elastoplastic seabed: A two-layered model. *International Journal for Numerical and Analytical Methods in Geomechanics*, 33(5): 591-610. https://doi.org/10.1002/nag.734

Logg, A., Mardal, K.-A., and Wells, G. N. (2012). Automated Solution of Differential Equations by the Finite Element Method. Berlin, Heidelberg: Springer. https://doi.org/10.1007/978-3-642-23099-8

Miyamoto, J., Sassa, S. and Sekiguchi, H. (2004). Progressive solidification of a liquefied sand layer during continued wave loading. *Geotechnique* 54(10): 617-629. https://doi.org/10.1680/geot.2004.54.10.617

Rothschink, J., Karl, F., Stelzer, O. (2026). Soil liquefaction triggered by ship waves in rivers and canals A laboratory investigation on fine sands. *Proceedings of the 11th International Conference on Physical Modelling in Geotechnics.*

Rothschink, J. and Stelzer, O. (2022). Ship Wave induced Excess Pore Water Pressure in Riverbeds and Banks – an Investigation on Silty Sands. *River Flow 2022*: 301-308, CRC Press.

Sakai, T., Hatanaka, K., Mase, H. (1992). Wave-induced effective stress in seabed and its momentary liquefaction. *Journal of Waterway, Port, Coastal, and Ocean Engineering*, 118(2): 202-2026. https://doi.org/10.1061/(ASCE)0733-950X(1992)118:2(202)

Van der Hoef, M. A., Beetstra, R. and Kuipers, J.A.M. (2005). Lattice-Boltzmann simulations of low-Reynolds-number flow past mono- and bidisperse arrays of spheres: results for the permeability and drag force. *Journal of Fluid Mechanics*, 528: 233-254. https://doi.org/10.1017/S0022112004003295

Ye, J., Jeng, D., Ren, W., Changqi, Z. (2015). Numerical simulation of the wave-induced dynamic response of poro-elastoplastic seabed foundations and a composite breakwater. *Applied Mathematical Modelling,* 39(1). https://doi.org/10.1016/j.apm.2014.05.031